



Application of Large-Scale 3D Non-Orthogonal Boundary Fitted Sediment Transport Model and Small-Scale Approach for Offshore Structure in Cimanuk Delta North Java Sea

Muslim Muin*, Krisnaldi Idris & Nita Yuanita

Ocean Engineering Research Group, Faculty of Civil and Environmental Engineering
Institut Teknologi Bandung, TP Rakhmat 3rd Floor
Jalan Ganesha 10, Bandung 40132, Indonesia
*E-mail: m_muin@ocean.itb.ac.id

Abstract. The morphology of the Cimanuk Delta at the North Java Sea has changed rapidly over the last two decades. The annual sediment deposition is about two million cubic meters (Yuanita and Tingsanchali, [1]). The large-scale ocean hydrodynamics and sediment transport model *MuSed3D* (Muin, [2]) was applied to the North Java Sea to simulate suspended sediment transport at the study site. A potential offshore structure was positioned at approximately 30 km from the Cimanuk Delta. The result of the large-scale model was calibrated using observation data and Landsat satellite image interpretation. The agreement between the modeling results and the observations was excellent. It was found that the critical shear stresses for erosion and deposition were 0.1 Pa and 0.05 Pa respectively. An empirical formula was further utilized to assess the local scouring at the potential offshore structure site in a small-scale domain and under extreme conditions.

Keywords: *Cimanuk; model; MuSed3D; non-orthogonal boundary fitted; ocean hydrodynamics; sediment transport.*

1 Introduction

The Cimanuk River is located in West Java, Indonesia. The area of study is presented in Figure 1. The Java Sea is a shallow sea: the mean water depth is about 40 meter. The morphology of the Cimanuk Delta has changed rapidly because of high sediment loading in the Cimanuk River. The Java Sea is influenced by two monsoons, the West Monsoon (December-February) and the East Monsoon (May-September). The West Monsoon is also the wet season characterized by high rainfall.

Yuanita and Tingsanchali [1] have studied the morphological change of the Cimanuk Delta using the two-dimensional flow model *Mike21 HD* [1]. They found that the formation of the Cimanuk Delta was dominated by a large amount of sediment supplied from the Cimanuk River to the Java Sea. Most of

Received October, 27th, 2015, 1st Revision December 16th, 2015, 2nd Revision July 15th, 2016, Accepted for publication July 21st, 2016.

Copyright ©2016 Published by ITB Journal Publisher, ISSN: 2337-5779, DOI: 10.5614/j.eng.technol.sci.2016.48.3.5

MuSed3D simulates both non-cohesive and cohesive sediment. The mean discharge of sediment from the Cimanuk River is specified in the same order as a previous study by Yuanita and Tingsanchali [1]. However, the present study used a different open boundary condition, which appears to be a significant factor, in order to match the observation data from Landsat satellite image interpretation.

2 Far Field Model Description MuSed3D

Anticipating the use of a hydrodynamic model with substantial variation in latitude, Spaulding [3] developed a boundary fitted spherical coordinate model and solved vertically averaged equations of motion using Leendertsee's [4] multi-operational method in curvilinear coordinates. Muin [5] further improved the model by transforming both the dependent variables (the velocity components) as well as the independent variables (coordinate geometry) into curvilinear coordinates and introducing a three-dimensional solution using a split technique in which the governing equations are divided into an exterior (vertically averaged) and an interior mode (vertical structure). Anticipating the importance of mangroves as a driving force, Muin [6] included the water exchange between wet/dry areas and the main channel in the computation. Muin and Wurjanto [7] applied the vertically averaged version of the model to simulate tsunami and sediment transport in Aceh, Indonesia. Muin [8] integrated the lagrangian sediment transport model to simulate drilling, cutting and mud dispersion in Bituni Bay, Indonesia.

The mathematical basis for the model begins with continuity and momentum equations. Both equations were developed with the underlying assumption that the flow is incompressible, variation of water mass density is negligible except when multiplied with the earth's gravity (Boussinesq approximation), and vertical acceleration is negligible as compared to gravitational acceleration (hydrostatic approximation).

As boundary condition along the shoreline, the beach is assumed as impermeable surface where there is no fluid particle velocity normal to it. Time varying water surface elevation commands the boundary condition on the ocean side. Influxes from rivers may be included by specifying their discharge. Two options are available to specify shear stresses at the bottom: (1) quadratic stress law or (2) Manning coefficient. At the free surface, the wind stress is calculated using quadratic approximation.

In order to perform computation in a curvilinear system where the mesh is made up of square grids, both dependent and independent variables in the above three equations are transformed into a curvilinear coordinate system. The equations of

mass conservation (continuity) and motion in the (ξ, η) curvilinear system written in terms of contravariant velocity components are as follows.

Continuity in Eq. (1):

$$Jr \cos \theta \frac{\partial \xi}{\partial t} + \frac{\partial}{\partial \xi} (\cos \theta J u^c D) + \frac{\partial}{\partial \eta} (\cos \theta J v^c D) + Jr \cos \theta \frac{\partial (\omega D)}{\partial \sigma} = \frac{Q_R}{r} \quad (1)$$

Momentum equations in Eqs. (2) and (3):

▪ ξ -direction

$$\begin{aligned} \frac{\partial u^c D}{\partial t} = & -\frac{\theta_\eta \theta_\eta + \cos^2 \theta \phi_\eta \phi_\eta}{J^2 \rho_0 r \cos^2 \theta} \frac{Dg}{2} \left[\{\lambda + (\rho_s - 2\rho)(1 - \sigma)\} \frac{\partial D}{\partial \xi} + (4\rho - 2\rho_s) \frac{\partial \xi}{\partial \xi} + D \frac{\partial \lambda}{\partial \xi} \right] \\ & + \frac{\theta_\xi \theta_\eta + \cos^2 \theta \phi_\xi \phi_\eta}{J^2 \rho_0 r \cos^2 \theta} \frac{Dg}{2} \left[\{\lambda + (\rho_s - 2\rho)(1 - \sigma)\} \frac{\partial D}{\partial \eta} + (4\rho - 2\rho_s) \frac{\partial \xi}{\partial \eta} + D \frac{\partial \lambda}{\partial \eta} \right] \\ & - \frac{\theta_\eta}{J^2 r \cos^2 \theta} \left[\frac{\partial}{\partial \xi} (\phi_\xi \cos^2 \theta J u^c u^c D + \phi_\eta \cos^2 \theta J u^c v^c D) + \frac{\partial}{\partial \eta} (\phi_\xi \cos^2 \theta J u^c v^c D + \phi_\eta \cos^2 \theta J v^c v^c D) \right] \\ & + \frac{\phi_\eta}{J^2 r \cos^2 \theta} \left[\frac{\partial}{\partial \xi} (\theta_\xi \cos^2 \theta J u^c u^c D + \theta_\eta \cos^2 \theta J u^c v^c D) + \frac{\partial}{\partial \eta} (\theta_\xi \cos^2 \theta J u^c v^c D + \theta_\eta \cos^2 \theta J v^c v^c D) \right] \\ & - \frac{\partial}{\partial \sigma} (\omega u^c D) + \frac{fD}{J \cos \theta} \left[(\theta_\xi \theta_\eta + \cos^2 \theta \phi_\xi \phi_\eta) u_c + (\theta_\eta \theta_\eta + \cos^2 \theta \phi_\eta \phi_\eta) v_c \right] + \frac{4}{D} \frac{\partial}{\partial \sigma} \left(A_v \frac{\partial u^c}{\partial \sigma} \right) \end{aligned} \quad (2)$$

▪ η -direction

$$\begin{aligned} \frac{\partial v^c D}{\partial t} = & \frac{\theta_\eta \theta_\xi + \cos^2 \theta \phi_\eta \phi_\xi}{J^2 \rho_0 r \cos^2 \theta} \frac{Dg}{2} \left[\{\lambda + (\rho_s - 2\rho)(1 - \sigma)\} \frac{\partial D}{\partial \xi} + (4\rho - 2\rho_s) \frac{\partial \xi}{\partial \xi} + D \frac{\partial \lambda}{\partial \xi} \right] \\ & - \frac{\theta_\xi \theta_\xi + \cos^2 \theta \phi_\xi \phi_\xi}{J^2 \rho_0 r \cos^2 \theta} \frac{Dg}{2} \left[\{\lambda + (\rho_s - 2\rho)(1 - \sigma)\} \frac{\partial D}{\partial \eta} + (4\rho - 2\rho_s) \frac{\partial \xi}{\partial \eta} \right] \\ & + \frac{\theta_\xi}{J^2 r \cos^2 \theta} \left[\frac{\partial}{\partial \xi} (\phi_\xi \cos^2 \theta J u^c u^c D + \phi_\eta \cos^2 \theta J u^c v^c D) + \frac{\partial}{\partial \eta} (\phi_\xi \cos^2 \theta J u^c v^c D + \phi_\eta \cos^2 \theta J v^c v^c D) \right] \\ & - \frac{\phi_\xi}{J^2 r \cos^2 \theta} \left[\frac{\partial}{\partial \xi} (\theta_\xi \cos^2 \theta J u^c u^c D + \theta_\eta \cos^2 \theta J u^c v^c D) + \frac{\partial}{\partial \eta} (\theta_\xi \cos^2 \theta J u^c v^c D + \theta_\eta \cos^2 \theta J v^c v^c D) \right] \\ & - \frac{\partial}{\partial \sigma} (\omega v^c D) - \frac{fD}{J \cos \theta} \left[(\theta_\xi \theta_\xi + \cos^2 \theta \phi_\xi \phi_\xi) u_c + (\theta_\xi \theta_\eta + \cos^2 \theta \phi_\xi \phi_\eta) v_c \right] + \frac{4}{D} \frac{\partial}{\partial \sigma} \left(A_v \frac{\partial v^c}{\partial \sigma} \right) \end{aligned} \quad (3)$$

In addition, the equation for conservation of substance and the equation of state are also required to take into account sediment, salinity, and temperature. These equations are as shown in Eqs. (4) and (5).

Conservation of substance:

$$\frac{\partial q}{\partial t} + \frac{u^c}{r} \frac{\partial q}{\partial \xi} + \frac{v^c}{r} \frac{\partial q}{\partial \eta} + \omega \frac{\partial q}{\partial \sigma} = \frac{4}{D^2} \frac{\partial}{\partial \sigma} \left(D_v \frac{\partial q}{\partial \sigma} \right) + \frac{D_h}{r^2 J^2} \left[\left(\frac{\theta_\eta \theta_\eta}{\cos^2 \theta} + \phi_\eta \phi_\eta \right) \frac{\partial^2 q}{\partial \xi^2} - 2 \left(\frac{\theta_\xi \theta_\eta}{\cos^2 \theta} + \phi_\xi \theta_\eta \right) \frac{\partial^2 q}{\partial \xi \partial \eta} + \left(\frac{\theta_\xi \theta_\xi}{\cos^2 \theta} + \phi_\xi \phi_\xi \right) \frac{\partial^2 q}{\partial \eta^2} \right] \quad (4)$$

Conservation of suspended sediment:

$$\frac{\partial \Omega^n}{\partial t} + \frac{u^c}{r} \frac{\partial \Omega^n}{\partial \xi} + \frac{v^c}{r} \frac{\partial \Omega^n}{\partial \eta} + (\omega - \omega_s^n) \frac{\partial \Omega^n}{\partial \sigma} = \frac{4}{D^2} \frac{\partial}{\partial \sigma} \left(D_v \frac{\partial \Omega^n}{\partial \sigma} \right) + \frac{D_h}{r^2 J^2} \left[\left(\frac{\theta_\eta \theta_\eta}{\cos^2 \theta} + \phi_\eta \phi_\eta \right) \frac{\partial^2 \Omega^n}{\partial \xi^2} - 2 \left(\frac{\theta_\xi \theta_\eta}{\cos^2 \theta} + \phi_\xi \phi_\eta \right) \frac{\partial^2 \Omega^n}{\partial \xi \partial \eta} + \left(\frac{\theta_\xi \theta_\xi}{\cos^2 \theta} + \phi_\xi \phi_\xi \right) \frac{\partial^2 \Omega^n}{\partial \eta^2} \right] \quad (5)$$

+Erosionⁿ

Equation of state is given by Eq. (6):

$$\rho = \text{function of } (S, \Theta) \quad (6)$$

where:

- ξ, η = curvilinear coordinates
- t = time
- f = Coriolis parameter
- g = gravitational acceleration
- ρ' = vertical density difference ($\rho = \bar{\rho} + \rho'$)
- $\bar{\rho}$ = vertically-averaged mass density of water
- ρ_o = basin-averaged mass density of water
- ρ_s = water density at the surface
- ω = vertical velocity in σ -coordinate
- ω_s = settling velocity in σ -coordinate
- σ = sigma stretching coordinate
- ζ = water surface deviation from mean level
- h = water depth
- D = $h + \zeta$
- D_h = horizontal eddy diffusivity

$$\begin{aligned}
R &= \text{earth's radius} \\
\tau_s &= \text{surface shear stress} \\
\tau_b &= \text{bottom shear stress} \\
S &= \text{salinity} \\
\Theta &= \text{temperature in centigrade} \\
q &= \text{concentration of conservative substance such as } S \text{ or } \Theta \\
\Omega^n &= \text{concentration of } n\text{-th class of suspended sediment} \\
u^c, v^c &= \text{contravariant velocities} \\
Q_r &= \text{river flow} \\
J &= \text{Jacobian} \\
\lambda &= \int_{\sigma}^1 \rho d\sigma
\end{aligned}$$

The relationship between the contravariant velocities (u^c, v^c) and velocities in spherical coordinates (u, v) is given by Eqs. (7) and (8):

$$u = \cos\theta \phi_{\xi} u^c + \cos\theta \phi_{\eta} v^c \quad (7)$$

$$v = \theta_{\xi} u^c + \theta_{\eta} v^c \quad (8)$$

The above governing equations are solved numerically using a semi-implicit technique where the water surface elevation in the long wave equation is solved implicitly and the other variables explicitly. By adopting this combination, the time-step size in the numerical solution is not constrained by the shallow water wave celerity, hence facilitating rapid computer execution. A detailed description of the hydrodynamics model can be found in Muin [5].

The transport of suspended sediment was based on the three-dimensional model using Eq. (5). The sediment was divided into n classes, which can be cohesive or non-cohesive sediment. The properties of cohesive sediment are quite different from those of non-cohesive sediment. For cohesive sediment, which rarely settles as individual particles, the settling velocity is proportional to the concentration of sediment and salinity. The settling velocity was obtained from laboratory experiment.

Sediment Deposition:

The equation for sediment deposition is as in Eqs. (9) and (10):

$$\frac{dm_d}{dt} = \omega_s C \left(1 - \frac{\tau_b}{\tau_d} \right) \quad \text{for} \quad \frac{\tau_b}{\tau_d} < 1 \quad (9)$$

$$\frac{dm_d}{dt} = 0 \quad \text{for} \quad \frac{\tau_b}{\tau_d} > 1 \quad (10)$$

where:

$$\begin{aligned} \frac{dm_d}{dt} &= \text{rate of sediment deposition} \\ C &= \text{sediment concentration at the bottom} \\ \tau_b &= \text{water shear stress at the bottom} \\ \tau_d &= \text{critical velocity for deposition} \\ \omega_s &= \text{settling velocity} \end{aligned}$$

Sediment Erosion

The equation for sediment erosion is as in Eqs. (11) and (12):

$$\text{Erosion}^n = E_o \left(\left(\frac{\tau_b}{\tau_e} \right)^k - 1 \right) \rho_s / h_{cell} \quad \text{for} \quad \frac{\tau_b}{\tau_e} > 1 \quad (11)$$

$$\text{Erosion}^n = 0 \quad \text{for} \quad \frac{\tau_b}{\tau_e} < \text{or} = 1 \quad (12)$$

where:

$$\begin{aligned} \text{Erosion}^n &= \text{rate of sediment erosion} \\ \tau_e &= \text{critical shear stress for erosion} \\ E_o &= \text{erosion rate coefficient} \end{aligned}$$

3 Near Field Model Description

In the near field analysis, local scouring for a single vertical pile focused on the development of the maximum scour depth over time. The present knowledge on scour development is mainly based on small-scale laboratory tests. Scour around a vertical pile is caused by two mechanisms: horseshoe vortices at the upstream side of the pile and lee-wake vortices at the downstream side. The vortices are generated due to the seabed boundary layer of the incoming flow interacting with the adverse pressure gradient caused by the presence of the pile. The flow rotates away from surface of the pile, creating the horseshoe vortices around the pile. Figure 2 shows a definition sketch of a vertical pile in a flow.

Several formulas are available for scour prediction, some have been frequently referred to and some are considered as recent or more comprehensive.

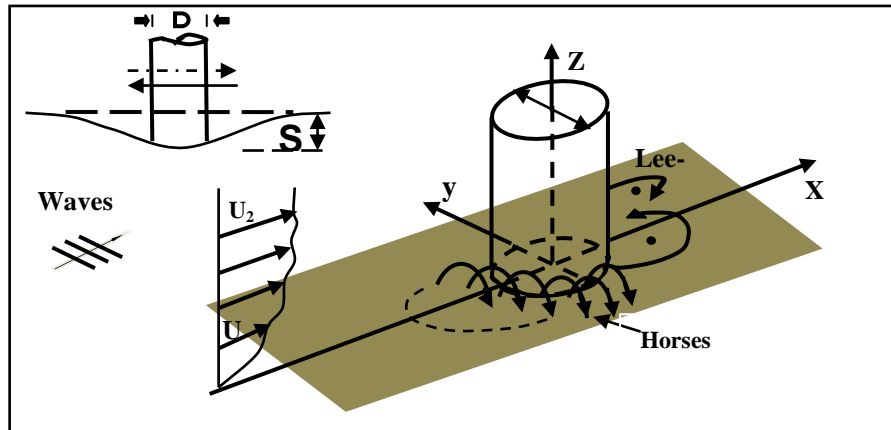


Figure 2 Definition sketch of a vertical pile in a flow, taken from Sumer and Fredsøe [9].

• Scouring Classification

Following Sumer and Fredsøe [9], local scour can be divided into two types: clear-water scour and live-bed scour, in which the classification is determined through the Shields parameter, θ . Clear-water scour happens when $\theta < \theta_{CR}$, in which case the shear force is not large enough to initiate any sediment motion on the seabed far from the structure, thus there is no movement of the bed material in the flow upstream. Live-bed scour is reached when $\theta > \theta_{CR}$ and the sediments will be transported over the entire seabed. It is common to assume that $\theta_{CR} \approx 0.05$. The Shield parameter can be written as in Eq. (13):

$$\theta = \frac{\tau_{\omega}}{\rho g (s - 1) d_{50}} \quad (13)$$

where,

s = ratio between sediment density ρ_s and fluid density ρ .

d_{50} = seabed median grain diameter

$\tau_{\omega} = \frac{1}{2} f_w U_m^2$ bed shear stress far away from the structure in the undisturbed flow

$f_w = c \left(\frac{a}{z_0} \right)^{-d}$ friction factor

U_m = maximum wave particle velocity at the seabed

- a = amplitude of the wave particle path
- z_0 = seabed roughness, given as $d_{50}/12$

The c and d parameters are defined as below:

Table 1 Parameters c and d [10].

c	d	Requirement
18.0	1.0	$20 \leq a/z_0 \leq 200$
1.39	0.52	$200 \leq a/z_0 \leq 11000$
0.112	0.25	$11000 \leq a/z_0$

• **Scour Depth in Regular Waves**

Sumer and Fredsøe [9], after reanalyzing a significant amount of secondary data (mostly related to non-breaking situations), provide an empirical formula for the equilibrium scour depth in regular waves, applicable for live-bed conditions, which can be written as:

$$\frac{S}{D} = 1.3[1 - \text{Exp}\{-0.03(KC - 6)\}] \tag{14}$$

where,

S = scour depth

D_p = pile diameter

KC = Keulegan-Carpenter Number = $\frac{U_m \cdot T}{D}$

T = wave period

It should be noted that the equation shows increasing scour depth with higher KC number, and for $KC \rightarrow \infty$, which can be interpreted as a steady current, S/D_p will approach 1.3.

• **Scour Depth in Regular Waves and Currents**

Sumer and Fredsøe [9], based on laboratory model testing, also provide a scour formula for cylindrical vertical piles that accounts for waves and currents. The formula provides the scour depth for a slender pile ($D/L < 0.2$, L = wave length) and applicable for live-bed conditions. The design formula for the maximum scour depth can be written as:

$$\frac{S_{\max}}{D} = \frac{S_c}{D} [1 - \text{Exp}\{-A \cdot (KC - B)\}] \tag{15}$$

$$A = 0.03 + 0.75 \cdot U_{CW}^{2.6} \quad B = 6 \cdot \text{Exp}(-7.4 \cdot U_{CW})$$

$$\text{and } U_{CW} = \frac{U_C}{U_C + U_m}$$

U_C is the steady current, and S_C is the scour depth due to the current alone. The conditions are similar as in the previous equation, where scour depth increases for a larger KC number.

4 Far Field Model Setup

The computational Non-Orthogonal Boundary Fitted Grid System is shown in Figure 3. The bathymetric data were obtained from Geodas. To minimize the effect of the open boundaries on the model results, the best strategy is to locate the model boundaries as far away as possible. Along the open boundaries, the tidal components were obtained from the ORI World Tidal Model. There is no sediment flux during inflow along the open boundaries. The time series of wind data in the computational domain was obtained from the US National Oceanic and Atmospheric Administration (NOAA). The version used in this study was NCEP Reanalysis 2, NOAA/NCDC Blended Daily Sea Surface Winds, providing global coverage with a horizontal resolution of 1° .

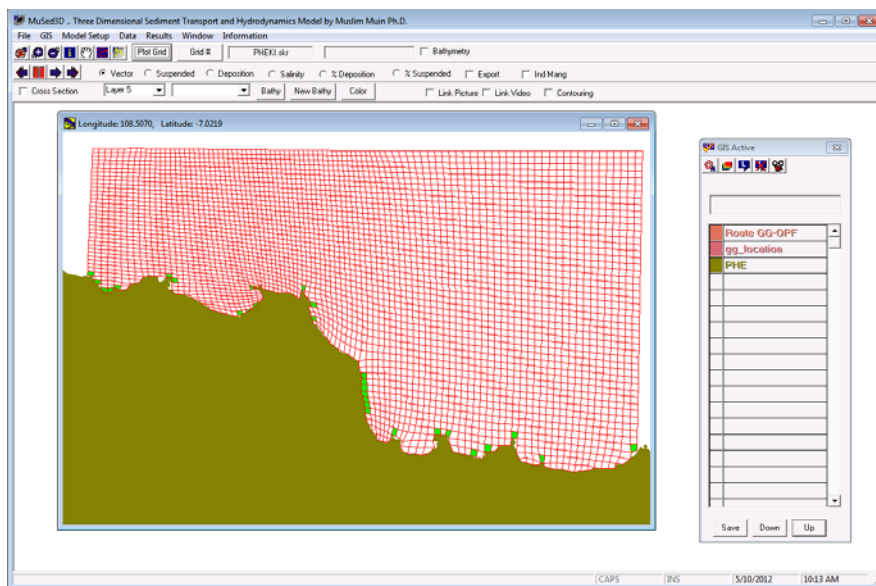


Figure 3 n-Orthogonal Boundary Fitted Grid System.

The river and sediment flux was obtained from the Ministry of Public Work Reports and Cimanuk Delta Study (Yuanita and Tingsanchali, [1]). The data were further normalized to obtain seasonal effects for projected time series data. The river and sediment flux from other rivers were based on the catchment area ratio.

5 Near Field Model Setup

The near field model was developed based on a suggestion by Sumer and Fredsøe [9]. The model was applied for representative wave conditions with wave steepness ranging from 0.033 to 0.076. The current data were adopted from hydrodynamic simulation, providing a range of current speeds from 0.42 m/sec to a maximum of 0.74 m/sec.

Prediction of local scouring around a vertical pile was conducted through an empirical formula suggested by Sumer [9]. Calculation was conducted for pile diameters ranging from 12 inch to 42 inch, in which the ratios of pile diameter to wavelength (D_p/L) were below 0.15, which shows the structure can be considered a small-size structure. The calculation of shield parameters showed that, for all flow conditions, the shield parameters were larger than the critical value of 0.05, thus the conditions can be considered live-bed and the empirical equation suggested by Sumer and Fredsøe [9] is applicable.

6 Far Field Model Calibration

The success of any model depends on the credibility of its predictions. This credibility is gained by careful comparison of model predictions with observations. The purpose of calibration is to select the model's coefficients to best match the observation data. The hydrodynamics model was calibrated by comparing the model's water level prediction and observations in Cirebon (Figure 4).

The quadratic bottom friction coefficients in the main water body were tuned to match the water elevation data. The sediment transport model was calibrated by comparing the Total Suspended Solid (TSS) concentration. The critical shear stress and erosion rate coefficients were tuned to match the observation data. The following parameter values were selected in the model: the quadratic bottom stress coefficient was 0.1, the critical shear stress for erosion and deposition were 0.1 Pa and 0.05 Pa respectively, and the erosion rate coefficient was 0.1 mm/hour.

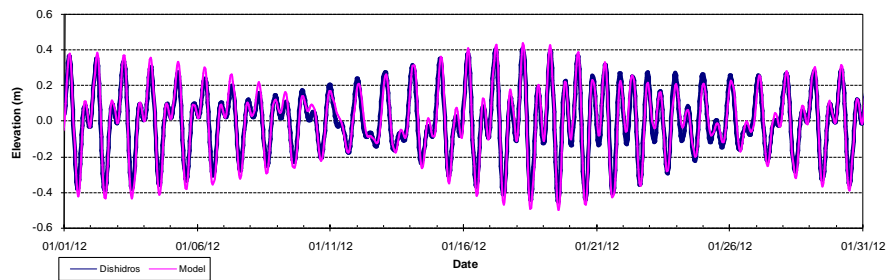


Figure 4 Comparison between model and observed water elevation at Cirebon Coast.

The spatial extent of sediment from Cimanuk River from the simulation was compared with Landsat Image Interpretation as presented in Figure 5. The TSS interpretation was done by Solihudin [11]. This study indicates that in the offshore region the TSS concentration ranges from 0 to 25 ppm, while the simulation results showed that the TSS concentration ranges from 20 to 40 ppm. The discrepancies are acceptable.

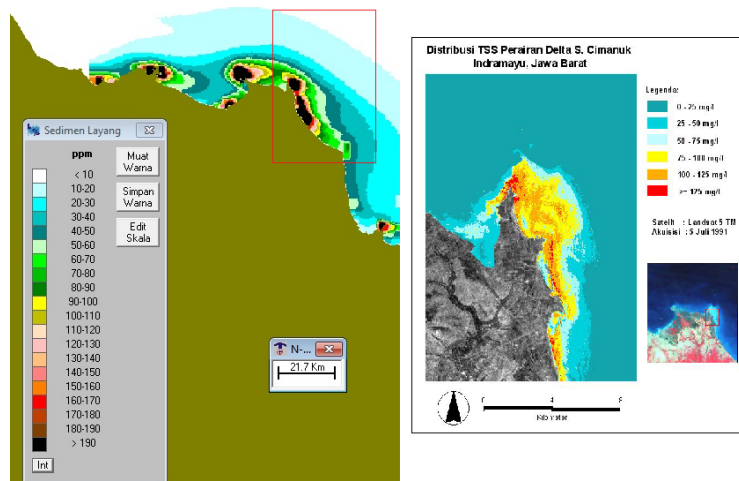


Figure 5 Comparison of TSS concentration between Landsat Image (Solihudin, [11]) and model predictions.

The TSS observation data in Subang Coast, Indramayu Coast and Cirebon Coast were used to validate the sediment transport model. The TSS concentration is higher in the West Monsoon than that in the East Monsoon, which is related to rainfall and ocean current direction. Comparisons between the model's prediction and observation data are presented in Figure 6 and

Figure 7, for West Monsoon and East Monsoon respectively. It can be seen that the prediction and observation were in good agreement. The results of the simulation were also compared with observation data from the Cimanuk Delta (Figure 8). The concentrations in these two locations are very high because of high sediment loading from the Cimanuk River. The observation data were obtained from the Cimanuk Delta study by Yuanita and Tingsanchali [1].

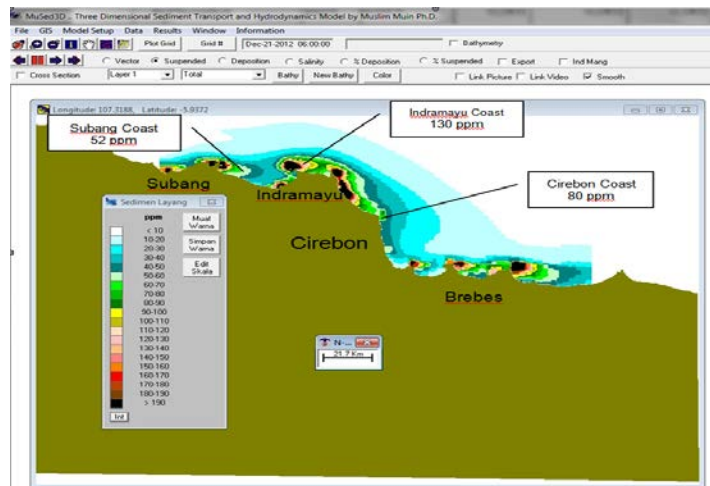


Figure 6 Comparison between model prediction and observation data during West Monsoon (December to February).

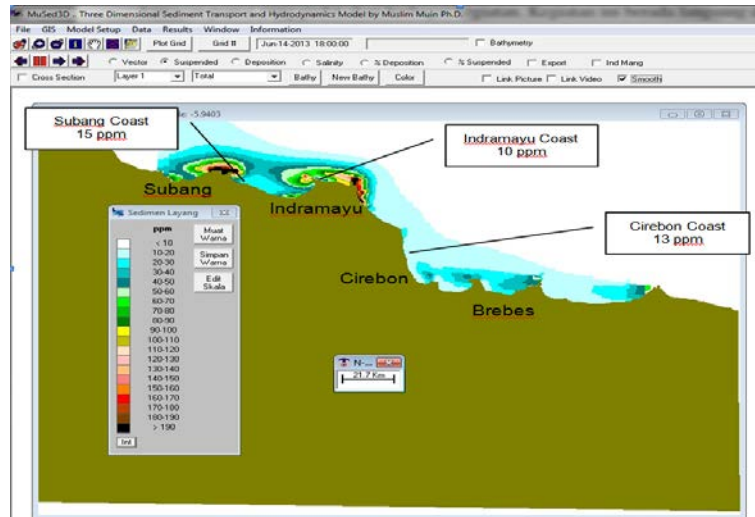


Figure 7 Comparison between model prediction and observation data during East Monsoon (May to September).

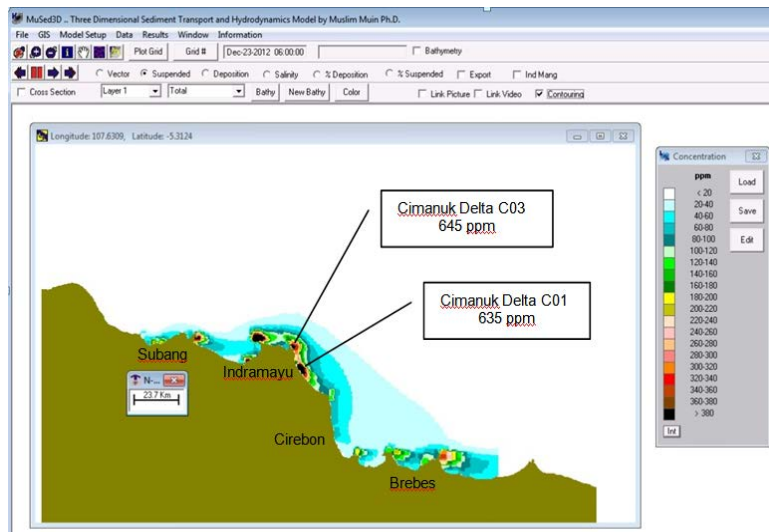


Figure 8 Comparison between model prediction and observation data in Cimanuk Delta during Wet Season.

7 Results of Far Field Simulation

The flow pattern during high and low tide are presented in Figures 9 and 10, for each season respectively. The results of the simulation indicate that the tidal and wind induced current is significant in the study area.

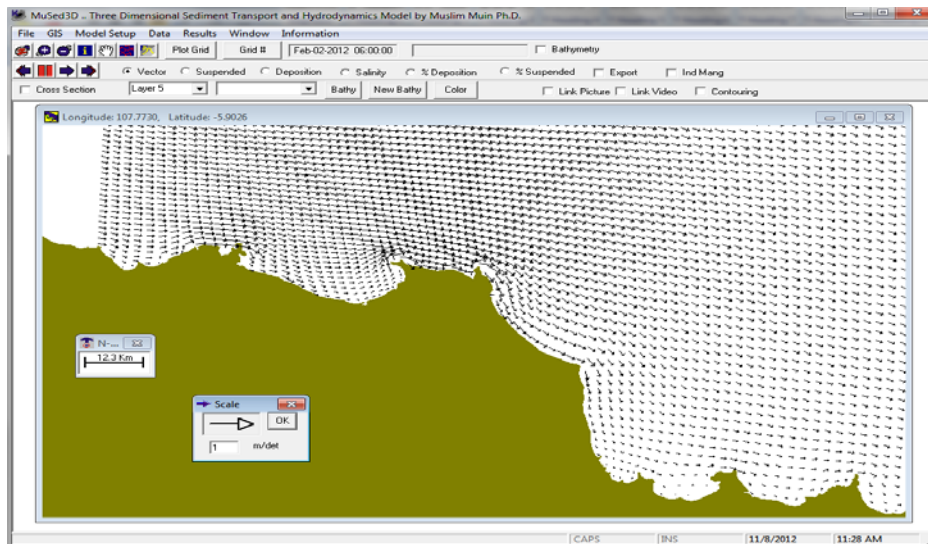


Figure 9 Flow pattern at low tide during West Monsoon.

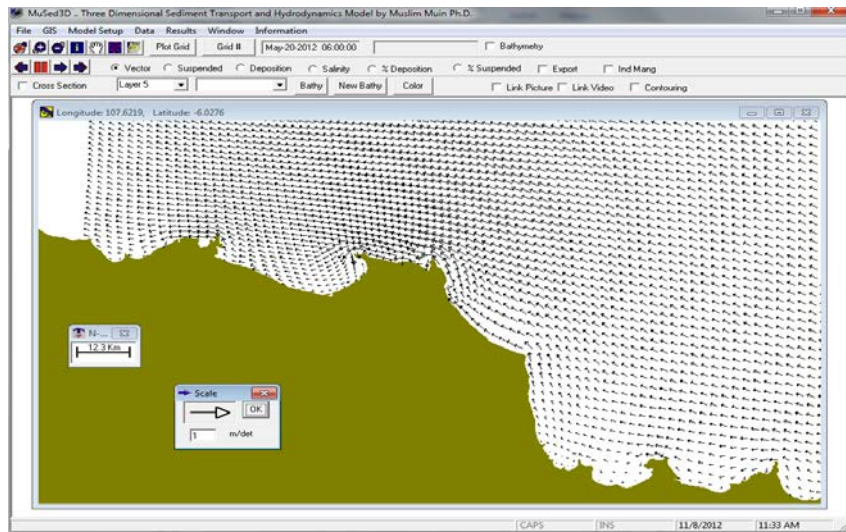


Figure 10 Flow pattern at high tide during East Monsoon.

The modeling results show that the currents are strong in the Cimanuk Delta because the flows are contracted in this region. The yearly maximum current at the study site is 0.4 m/s. The model was also run under an extreme wind with a 100-year return period. It was found that the maximum bottom current at the study site is 0.75 m/s. The spatial extent of sediment deposition is presented in Figure 11. The model indicated that the sediment is mostly deposited in the mouth of each delta of the rivers, with high sediment loading.

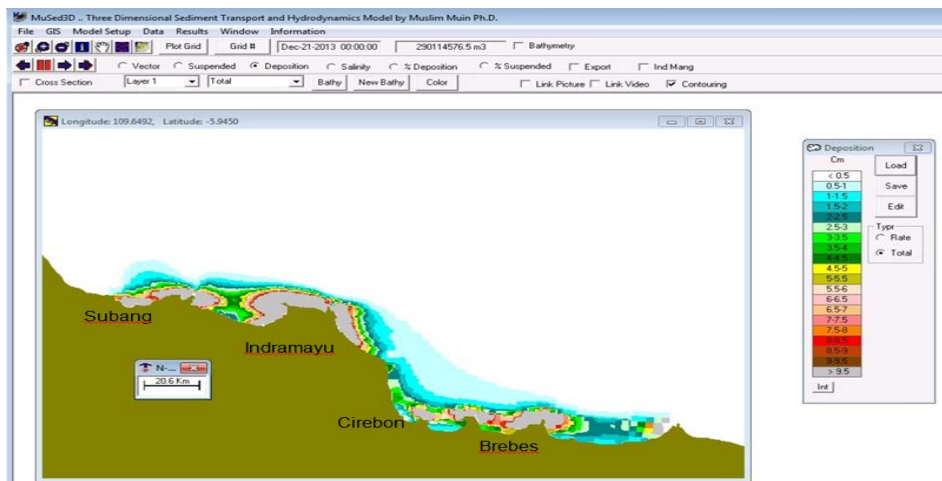


Figure 11 Sediment deposition (cm) after two-year simulation.

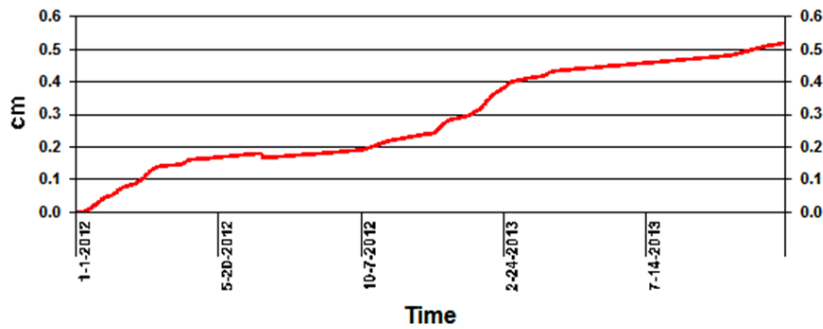


Figure 12 Time series of predicted sediment deposition at study site for two-year simulation.

Figure 12 and Figure 13 presents the time series of the sediment deposition and TSS concentration at the study site respectively. It shows that the deposition rate is 0.25 cm/year and TSS concentration ranged from 5 ppm to 40 ppm. The deposition rate and TSS concentrations are highest during the West Monsoon.

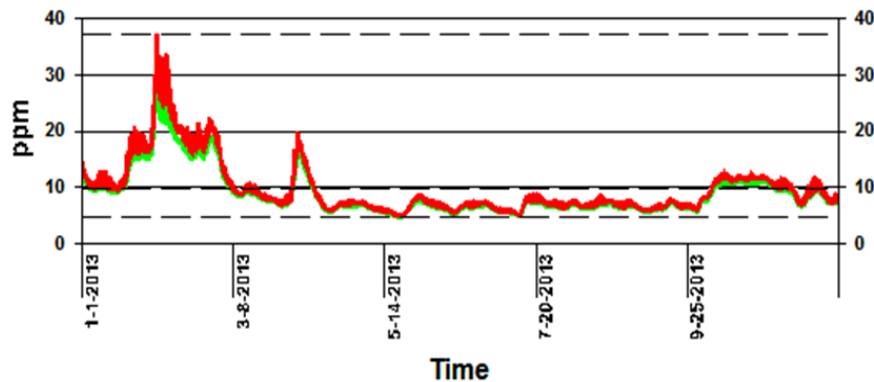


Figure 13 Time series of TSS concentration at study site.

8 Results of Near Field Simulation

The predicted scouring around a vertical pile due to wave motion is presented in Figure 14, which shows predicted scouring due to significant waves and maximum waves, each for a 1-year and a 100-year return period. Predicted scouring around a vertical pile due to wave motion and current is presented in Figure 15, which also shows predicted scouring due to significant waves and maximum waves, each for a 1-year and a 100-year return period.

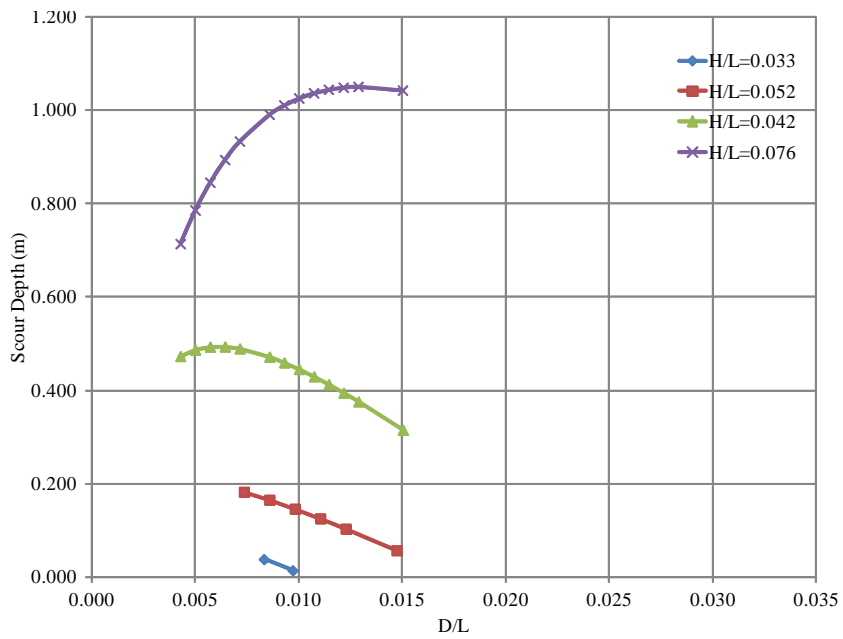


Figure 14 Scour depth around a vertical pile due to waves.

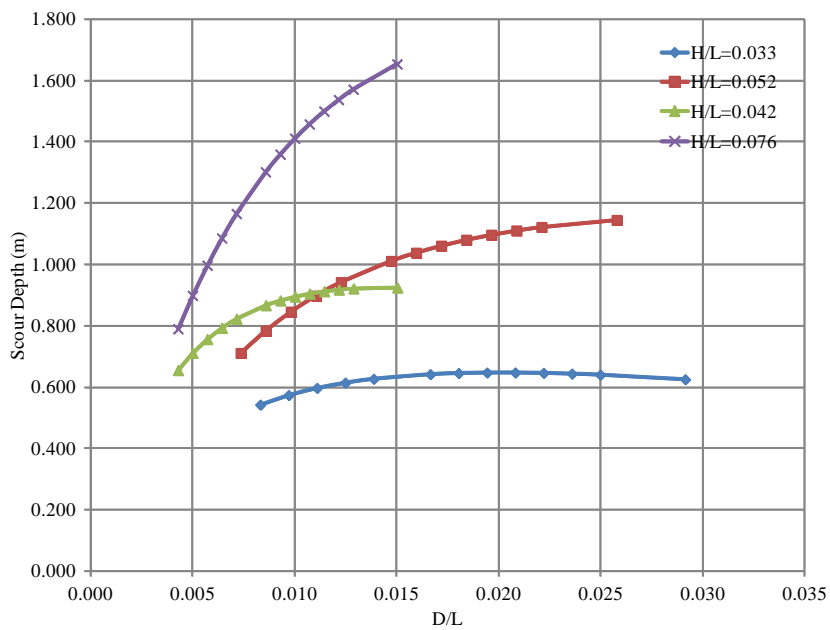


Figure 15 Scour depth around a vertical pile due to waves.

9 Conclusion

9.1 Far Field Analysis

The Three-Dimensional Ocean Hydrodynamics and Sediment Transport 3D Non-Orthogonal Boundary Fitted Model was successfully applied in the area of study. The model was calibrated by comparing field measurements and the results of a simulation for several stations. Comparison revealed that satellite image analysis and model predictions were in good agreement.

The ocean current in the area of study is strongly influenced by the Monsoon. The yearly maximum current at the study site is 0.4 m/s, while the 100-year maximum current is 0.74 m/s. Despite the TSS concentration in the Cimanuk Delta being very high (> 300 ppm), the TSS concentration at the study site only ranged from 5 ppm to 40 ppm, where the highest concentration occurred during the West Monsoon. This is consistent with satellite image interpretation of the area of study. The yearly sediment deposition rate at the study site is about 0.25 cm/year. The rate is much higher during the West Monsoon than the East Monsoon.

9.2 Near Field Analysis

For various pile diameters, the prediction of scour depth due to combination of waves and current obtained larger values compared to one, due to wave action only. The simulated maximum 100-year wind-generated current was a governing factor in the scouring depth results.

One-year return period significant waves combined with the current were predicted to cause a scour depth ranging from 0.53 m to 0.65 m, depending on pile diameter. The scour depth was almost constant as the diameter increased. 100-year significant waves combined with 100-year currents predicted to cause a scour depth ranging from 0.7 m to 1.1 m, depending on pile diameter.

A sizeable scour depth may occur due to 100-year return period waves and currents, depending on pile diameter, the scour depth varying from 0.78 m to 1.61 m.

References

- [1] Yuanita, N. & Tingsanchali, T., *Development of a River Delta: a Case Study of Cimanuk River Mouth, Indonesia*, Hydrological Processes, **22**, pp. 3785-3801. 2008.

- [2] Muin, M. & Spaulding, M., *Three-Dimensional Boundary-fitted Circulation Model*, J. Hydraulic Engineering, ASCE, **123**(1), pp. 2-11, 1997.
- [3] Spaulding, M.L., *A vertically-averaged circulation model using boundary fitted coordinates*. J. Physical Oceanography, **14**, pp. 973-982. 1984.
- [4] Leendertse, J.J., *Aspects of Computational Model for Long Period Water-Wave Propagation*. Report RM-5294-PR, Rand Corp., Santa Monica, CA, USA. 1967.
- [5] Muin, M., *A Three-Dimensional Boundary-Fitted Circulation Model in Spherical Coordinates*, PhD Dissertation, Department of Ocean Engineering, University of Rhode Island, 1993.
- [6] Muin, M., *Application of 3-D Boundary Fitted Hydrodynamics and Sediment Transport Model in ADA Estuary*, Interim Report 1, LAPI Institut Teknologi Bandung. 1999.
- [7] Muin, M. & Wurjanto, A., *Development and Application of Ocean Hydrodynamics and Sediment Transport Model Using Non-Orthogonal Curvilinear Spherical Coordinate Technique to Simulate Tsunami*, Proceedings of the Twenty-third International Offshore and Polar Engineering. Anchorage, Alaska, USA, June 30-July 5, 2013.
- [8] Muin, M., *Integration Lagrangian Sediment Transport into Non-Orthogonal Ocean Hydrodynamics Model to Simulate Drilling Cutting and Mud Dispersion in Indonesia Sea Water*, Proceedings of the Twenty-third International Offshore and Polar Engineering. Anchorage, Alaska, USA, June 30-July 5, 2013.
- [9] Summer M. & Fredsøe J., *The Mechanics of Scour in the Marine Environment*, *Advance Series in Ocean Engineering*, **17**, World Scientific, 2002.
- [10] Fredsøe J. & Degard, R., *The Mechanics of Coastal Sediment Transport*, *Advance Series in Ocean Engineering*, **8**, World Scientific, 1992.
- [11] Solihuddin, Tb., *Multi-Temporal Landsat Image Application for Monitoring the Concentrations of Total Suspended Solid in Cimanuk Delta Sea, West Java*, Bulletin of Environmental Geology, **19**(3), December 2009, pp. 107-116, 2009.